

W. van Westrenen · N. L. Allan · J. D. Blundy
M. Yu. Lavrentiev · B. R. Lucas · J. A. Purton

Trace element incorporation into pyrope–grossular solid solutions: an atomistic simulation study

Received: 27 January 2000 / Accepted: 14 February 2003

Abstract We have performed atomistic computer simulations on trace element incorporation into the divalent dodecahedral X-sites of pyrope (Py — $\text{Mg}_3\text{Al}_2\text{Si}_3\text{O}_{12}$) – grossular (Gr — $\text{Ca}_3\text{Al}_2\text{Si}_3\text{O}_{12}$) solid solutions. An ionic model and the Mott–Littleton two-region approach to defect energies were used to calculate the energetics of substitution by a range of divalent trace-elements and of charge-balanced substitution by trivalent ions in the static limit. Results are compared with experimental high-temperature, high-pressure garnet–melt trace element partitioning data obtained for the same garnet solid solution to refine our understanding of the factors controlling element partitioning into solid solutions. Defect energies ($U_{\text{def},f}$), relaxation (lattice strain) energies (U_{rel}), and solution energies (U_{sol}) were derived using two different approaches. One approach assumes the presence of one type of hybrid X-site with properties intermediate between pure Mg and Ca sites, and the other assumes discrete Mg and Ca X-sites, and thus two distinct cation sublattices. The hybrid model is shown to be inadequate, since it averages out local distortions in the garnet structure. The discrete model results suggest

trace elements are more soluble in $\text{Py}_{50}\text{Gy}_{50}$ than in either end-member compound. Physically this is due to small changes in size of the X-sites and the removal of unfavourable interactions between third nearest neighbours of the same size. Surprisingly, depending on the local order, large trace element cations may substitute for Mg^{2+} and small trace elements for Ca^{2+} in $\text{Py}_{50}\text{Gr}_{50}$. These solubilities provide an explanation for the anomalous trace-element partitioning behaviour along the pyrope–grossular join observed experimentally.

Keywords Element partitioning · Solid solutions · Garnet · Atomistic simulation

Introduction

Trace-element concentrations in igneous rocks and their constituent phases (minerals ± quenched melts) are widely used to develop and test petrogenetic models (e.g. Gast 1968; Shaw 1970; Shimizu 1975; Loubet and Allègre 1982; McKenzie and O’Nions 1991; Frey et al. 1994; Putirka 1999). An essential prerequisite for using trace elements in this fashion is the accurate knowledge of the partitioning behaviour of trace elements between minerals and co-existing melts. In recent years, our understanding of the principles governing the distribution of trace elements between solid and liquid phases has increased significantly. Rapid development of suitable analytical techniques has led to a large increase in partitioning data, while the advent of empirical models of mineral–melt partitioning (Beattie 1994; Blundy and Wood 1994) provides a convenient framework for their interpretation (e.g. Wood and Blundy 1997; Allan et al. 2001; Van Westrenen et al. 2001a).

Parallel to these advances, increases in computer speed and development of new algorithms have facilitated atomistic computer simulation studies of the incorporation of trace-elements in crystal structures. These are providing independent insights into the ener-

W. van Westrenen (✉) · J. D. Blundy
CETSEI, Department of Earth Sciences,
University of Bristol, Wills Memorial Building,
Bristol BS8 1RJ, UK
e-mail: willem.vanwestrenen@erdw.ethz.ch
Fax: +41-1-6321088
Tel.: +41-1-6324381

N. L. Allan · B. R. Lucas
School of Chemistry, University of Bristol,
Cantock’s Close, Bristol BS8 1TS, UK

M. Yu Lavrentiev
Institute of Inorganic Chemistry, 630090 Novosibirsk, Russia

J. A. Purton
CLRC, Daresbury Laboratory, Warrington,
Cheshire WA4 4AD, UK

Present address: W. van Westrenen
Institut für Mineralogie und Petrographie,
ETH Zürich, Sonneggstrasse 5, ETH Zentrum,
CH 8092, Switzerland

geetics of trace-element incorporation into the lattices of aluminosilicate minerals (e.g. Purton et al. 1996, 1997a, 2000; Van Westrenen et al. 2000a). Up to now, virtually all computational studies have dealt exclusively with trace elements entering pure end-member compositions such as forsterite and diopside (Purton et al. 1996, 1997a) and the garnet end members pyrope (Py — $\text{Mg}_3\text{Al}_2\text{Si}_3\text{O}_{12}$), grossular (Gr — $\text{Ca}_3\text{Al}_2\text{Si}_3\text{O}_{12}$), almandine ($\text{Fe}_3\text{Al}_2\text{Si}_3\text{O}_{12}$) and spessartine ($\text{Mn}_3\text{Al}_2\text{Si}_3\text{O}_{12}$) (Van Westrenen et al. 2000a). However, most natural samples are solid solutions, making an evaluation of the effects of solid solution formation and disorder on trace-element energetics highly desirable.

In this paper we report atomistic simulations of trace-element incorporation into the large dodecahedral X-site of pyrope–grossular solid solutions. Garnet solid solutions are stable over a wide range of pressures and temperatures in the Earth. The thermodynamic properties of garnet solid solutions have been the subject of numerous experimental studies (see, e.g. reviews by Geiger 1999, 2001), and more recently in the simulation studies of Bosenick et al. (2000, 2001) and Lavrentiev et al. (pers. comm.). Non-ideal behaviour is ubiquitous, particularly along the pyrope–grossular join for which large positive excess enthalpies, entropies and volumes of mixing have been reported (Geiger 1999). Interestingly, non-linearities are also observed in garnet mineral–melt partitioning data, as discussed below, and so in this paper we extend the previous simulation studies and consider trace-element incorporation. We compare results from our simulations with experimental observations in order to refine our understanding of the factors controlling element partitioning into garnets.

Recent partitioning models (Beattie 1994; Blundy and Wood 1994) are based on the observation of Onuma et al. (1968) that mineral–melt partition coefficients (D s) for series of isovalent trace-elements entering a specific crystal lattice site show a near-parabolic dependence on trace-element ionic radius. This is illustrated in Fig. 1a, showing three sets of garnet–melt partition coefficients, $D^{\text{Grt}/\text{Melt}}$, as a function of trace-element radius r , for trivalent trace elements entering the dodecahedral garnet X-site (Van Westrenen et al. 1999). The X-site, predominantly occupied by a mixture of Mg, Ca, Fe(II) and Mn in nature, is the favoured site for the rare-earth elements (REE), U and Th in garnet (e.g. Quartieri et al. 1999; Van Westrenen et al. 1999, 2000b). These trace elements are among the most important and widely used in petrogenetic models involving garnets (e.g. LaTourrette et al. 1993; Shen and Forsyth 1995; Hirschmann and Stolper 1996; Bourdon et al. 1996; Blichert-Toft et al. 1999). The three datasets in Fig. 1a represent garnet–melt partitioning experiments, performed at a constant pressure of 3 GPa and a near-constant temperature of $1545 \pm 15^\circ\text{C}$, on different bulk compositions in the simple system $\text{CaO–MgO–Al}_2\text{O}_3\text{–SiO}_2$ (CMAS). The experiments, aimed at isolating the influence of garnet Ca and Mg contents on $D^{\text{Grt}/\text{Melt}}$, produced garnets with widely different compositions along the Py–Gr join.

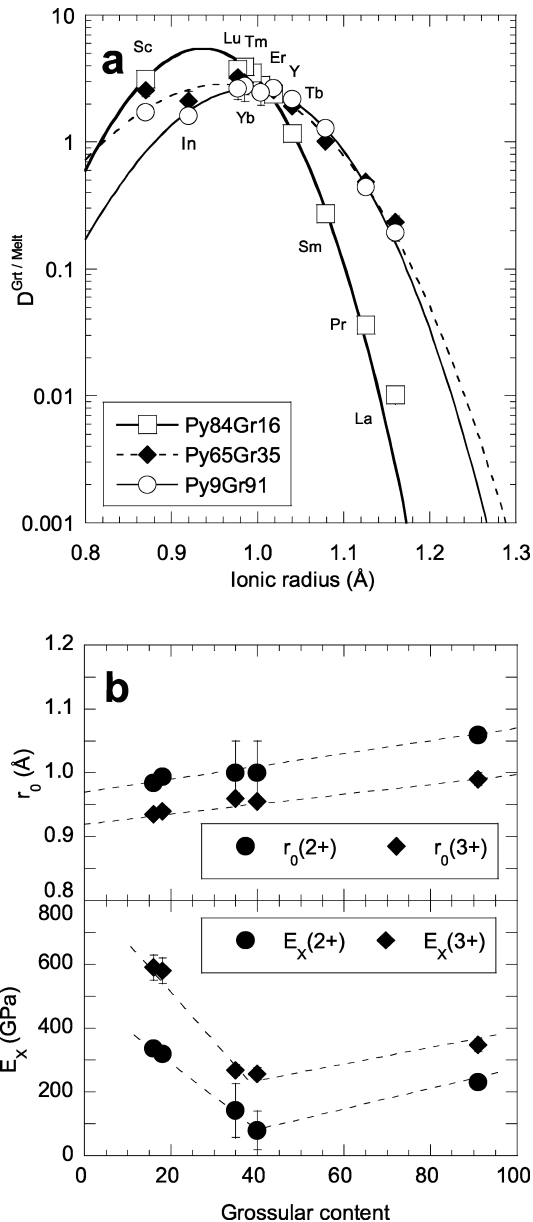


Fig. 1 a Experimental variation of garnet–melt partition coefficients ($D^{\text{Grt}/\text{Melt}}$) entering the garnet X-site. $D^{\text{Grt}/\text{Melt}}$ (defined as the concentration (in wt%) of an element in garnet divided by its concentration in coexisting melt) are shown for trivalent trace elements (REE, Y, In, Sc) in three high-pressure (3 GPa), high-temperature ($1545 \pm 15^\circ\text{C}$) experiments along the Py–Gr join. Curves are least-squares fits of Eq. (2) to data. Partitioning data for divalent elements not shown for clarity. **b** Variation of fitted values of $r_0(2+, 3+)$ (upper panel) and $E_X(2+, 3+)$ (lower panel) along the Py–Gr join. Note anomalous $E_X(2+)$ and $E_X(3+)$ for intermediate garnets. Partitioning data from Van Westrenen et al. (1999), ionic radii from Shannon (1976). 1σ error bars are smaller than symbol size

Blundy and Wood (1994) rationalized near-parabolic dependencies such as those shown in Fig. 1a using the lattice strain model of Brice (1975). Brice (1975) related the lattice strain energy, U_{strain} , associated with the insertion of a trace element with radius r_i into a site with radius r_0 , to the size misfit ($r_i - r_0$) between substituent and host cation. Per mole of trace element

$$U_{\text{strain}} = 4\pi EN_A \left[\frac{1}{2} r_0 (r_i - r_0)^2 + \frac{1}{3} (r_i - r_0)^3 \right], \quad (1)$$

where E is the Young's modulus and N_A Avogadro's constant. The larger the size misfit ($r_i - r_0$), or the higher the value of E , the larger is the strain energy associated with a substitution, and the lower is the affinity of the host structure for a particular trace element. Blundy and Wood (1994) assumed that, as crystals are far more rigid than melts, the energy associated with the exchange reaction between melt and crystal, and therefore the corresponding mineral-melt partition coefficient D can be approximated by the strain energy U_{strain} in the crystal. Thus,

$$\begin{aligned} D^{\text{mineral/melt}} &= D_0 \exp\left(-\frac{U_{\text{exchange}}}{RT}\right) \\ &\cong D_0 \exp\left(-\frac{U_{\text{strain}}}{RT}\right), \end{aligned} \quad (2)$$

where D_0 is a constant for any given P , T and melt composition. As can be seen from Eq. (2), the trace element that produces the largest strain energy upon incorporation in a mineral will have the lowest mineral-melt partition coefficient.

The curves drawn in Fig. 1a are fits to the experimental data obtained using Eqs. (1) and (2). Variations in mineral-melt partition coefficients with mineral composition can be described conveniently using the fitted parameters r_0 and E . Figure 1b shows the variations in r_0 and the "apparent" or "effective" Young's modulus E with garnet composition (along the pyrope–grossular join) for both trivalent and divalent elements. Values of r_0 show a systematic dependence on garnet composition, increasing linearly with increasing grossular content. This is entirely consistent with the crystallographically observed differences between the $\langle X-O \rangle$ bond lengths of pyrope (~ 2.27 Å; Armbruster et al. 1992) and grossular (~ 2.41 Å; Ganguly et al. 1993). On the other hand, the effective X-site modulus, E_X , shows profound non-linearity along the join, with E_X for intermediate pyrope–grossular garnets (Py₆₀Gr₄₀ in Fig. 1) lower than E_X for both pyrope- and grossular-rich garnets. This anomaly is observed in the data of Van Westrenen et al. (1999) for both trivalent and divalent elements (the latter not shown in Fig. 1a). Non-linear behaviour between Py- or Gr-rich and intermediate Py–Gr garnets is also observed in partitioning data for several other trace elements of key importance to petrogenetic models (e.g. Zr, Hf, Ti; Van Westrenen et al. 2001b), as well as in natural garnet–pyroxene partitioning data (e.g. Harte and Kirkley 1997).

These non-linearities are likely associated with the peculiarities of the garnet crystal structure. Figure 2 shows the structure of garnet as a set of interconnected polyhedra showing the X-site dodecahedra, together with the SiO₄ tetrahedra and AlO₆ octahedra. There is extensive edge-sharing between these polyhedra forming a three-dimensional network. Each tetrahedron shares

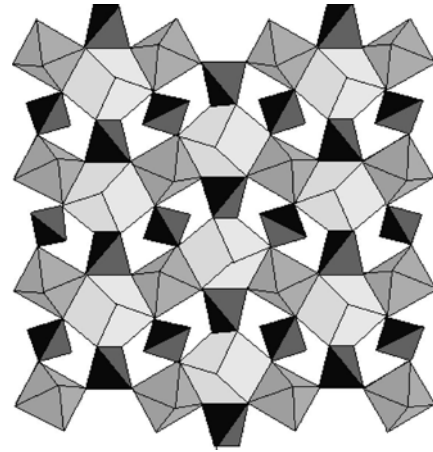


Fig. 2 Two-dimensional projection of the garnet structure (after Merli et al. 1995). Alternating isolated tetrahedra (black) and octahedra (dark grey) form a three-dimensional corner-sharing network, with the resulting cavities forming dodecahedra (light grey)

two opposite edges with dodecahedra, each dodecahedron shares four edges with other dodecahedra and every octahedron shares six edges with the surrounding dodecahedra. All polyhedra in the garnet structure are distorted from "ideal" geometry, and these distortions are likely to influence the energetic and structural behaviour of solid solutions. Accordingly, in this paper in addition to presenting results for a hybrid "mean-field" model in which all X-sites have the same properties, intermediate between those of Mg and Ca sites and dependent on bulk composition, we also carry out simulations based on discrete Mg and Ca sites, which do not average out local structural distortions.

The structure of this paper is as follows. In the next section we summarize the theoretical methods for perfect and defective lattices and discuss in detail the interatomic potentials used in our simulations. Results for the hybrid and discrete models are then presented in turn. The two sets of results are then compared, the importance of local ordering assessed and the implications for trace-element partitioning examined.

Methods and simulations of garnet structures

For all simulations a conventional Born ionic model was used, assigning integral ionic charges, based on accepted chemical valence rules, to all species (i.e. 2+ to Mg and Ca, 3+ to Al, 4+ to Si, and 2- to O). Cation–oxygen interactions were described by a consistent set of 2-body interionic Buckingham potentials, which take the form:

$$\varphi(r_{ij}) = A \exp\left(-\frac{r_{ij}}{\rho}\right) - \frac{C}{r_{ij}^6}, \quad (3)$$

with A , ρ and C constants derived from simulations on binary oxides, and r_{ij} the interionic distance. The oxide ion polarizability was taken into account using the shell model of Dick and Overhauser (1958), and a three-body O–Si–O bond bending term incorporated. Purton et al. (1996, 1997a) have shown the

applicability of these potentials for simulations of oxides (CaO and MgO) and silicates (olivine, orthopyroxene, clinopyroxene). Potentials for Si, Al and O, as well as Mg and Ca where these are present as discrete species, were identical to those used in our earlier study (Van Westrenen et al. 2000a).

All simulations were performed using the General Utility Lattice Program (GULP) of Gale (1997). Static simulations of perfect lattices (i.e. without any trace elements present) give the lattice energy and crystal structure at zero pressure of the garnets. In the static limit, the lattice structure is determined by the condition $\partial U/\partial x_i = 0$ where U is the internal energy in the absence of lattice vibrations, and the variables $\{X_i\}$ (the lattice vectors and basis atom coordinates) define the structure. No symmetry constraints were applied.

Table 1 gives a comparison of observed and computed lattice parameters for end members pyrope and grossular using these potentials. Agreement between experiment and simulation is satisfactory and in line with that obtained in other recent simulations on pyrope–grossular garnets (Bosenick et al. 2000). From a crystal-structural viewpoint, we note the change in sign of the difference in O–O distances between unshared and shared octahedral edges. Shared O–O edges are longer than unshared ones in grossular, but shorter than unshared ones in pyrope, as observed experimentally (Table 1). The data in Table 1 show that the potential set gives a sufficiently accurate description of garnet structures.

Hybrid model

In the hybrid model calculations, effective potentials for X-site cation–oxygen interactions in garnets were constructed following the method of Winkler et al. (1991), who use a mean-field approach. They derive effective, hybrid, potentials for sites occupied by more than one atom from a combination of the interionic potentials for the constituent species (in our case Mg and Ca). Under the assumption that the first and second derivatives of the hybrid interaction are equal to the weighted averages of the derivatives of the Mg–O and Ca–O interactions for the observed X–O bond length, Winkler et al. (1991) obtain:

$$\rho_{\text{eff}} = \frac{x_{\text{Mg}}\rho_{\text{Mg}}^{-1}A_{\text{Mg}}\exp(-R\rho_{\text{Mg}}^{-1}) + (1 - x_{\text{Mg}})\rho_{\text{Ca}}^{-1}A_{\text{Ca}}\exp(-R\rho_{\text{Ca}}^{-1})}{x_{\text{Mg}}\rho_{\text{Mg}}^{-2}A_{\text{Mg}}\exp(-R\rho_{\text{Mg}}^{-1}) + (1 - x_{\text{Mg}})\rho_{\text{Ca}}^{-2}A_{\text{Ca}}\exp(-R\rho_{\text{Ca}}^{-1})} \quad (4)$$

Table 1 Comparison between observed and simulated lattice parameters of end-member garnets

Property	Pyrope		Grossular	
	Observed ^a	Simulated	Observed ^b	Simulated (unit)
Unit-cell dimensions and oxygen atom coordinates				
<i>a</i>	11.452	11.281	11.848	11.874 (Å)
<i>b</i>	11.452	11.281	11.848	11.874 (Å)
<i>c</i>	11.452	11.281	11.848	11.874 (Å)
<i>x</i> (O)	0.0329	0.0318	0.0382	0.0385 –
<i>y</i> (O)	0.0503	0.0519	0.0453	0.0458 –
<i>z</i> (O)	0.6533	0.6519	0.6514	0.6493 –
Dodecahedron (X-site)				
X–O(1)	2.197	2.168	2.322	2.331 (Å)
X–O(2)	2.340	2.283	2.487	2.542 (Å)
<X–O>	2.269	2.225	2.405	2.437 (Å)
O4–O6	2.708	2.649	2.971	3.076 (Å)
O4–O7	2.778	2.721	2.859	2.923 (Å)
Octahedron (Y-site)				
Al–O	1.886	1.846	1.926	1.894 (Å)
O1–O4 shared	2.617	2.541	2.758	2.747 (Å)
O1–O5 unshared	2.716	2.678	2.689	2.613 (Å)
Tetrahedron (Z-site)				
Si–O	1.634	1.635	1.646	1.649 (Å)
O1–O2	2.497	2.505	2.572	2.580 (Å)
O1–O3	2.751	2.749	2.745	2.743 (Å)

^a Lattice parameters for pyrope from Armbruster et al. (1992)

^b Lattice parameters for grossular from Ganguly et al. (1993)

$$A_{\text{eff}} = \frac{x_{\text{Mg}}\rho_{\text{Mg}}^{-1}A_{\text{Mg}}\exp(-R\rho_{\text{Mg}}^{-1}) + (1 - x_{\text{Mg}})\rho_{\text{Ca}}^{-1}A_{\text{Ca}}\exp(-R\rho_{\text{Ca}}^{-1})}{\rho_{\text{eff}}^{-1}\exp(-R\rho_{\text{eff}}^{-1})} \quad (5)$$

In these equations, x_{Mg} is the mole fraction of Mg ions on the X-site, and for any intermediate garnet R is the equilibrium or mean X–O bond length predicted from proportional addition of pyrope and grossular X–O bond lengths (taken from Merli et al. 1995; see also Smyth and Bish 1988). Calculated potential parameters for $x_{\text{Mg}} = 0.25, 0.50$ and 0.75 are given in Table 2. The analogous coefficient for the r^{-6} term in Eq. (3), C_{eff} , is zero for all compositions.

Discrete model

Simulations of solid solutions with discrete Mg and Ca sites were carried out for compositions Py₉₆Gr₄, Py₅₀Gr₅₀ and Py₄Gr₉₆. Following ²⁹Si MAS NMR studies (Bosenick et al. 1995, 1999) suggesting limited short-range Ca–Mg ordering in intermediate Py–Gr garnets, possible orderings along the join have been examined computationally (Bosenick et al. 2000; Lavrentiev pers. comm.). A particularly interesting conclusion of these studies is that by far the strongest repulsion of like cations (Ca–Ca, and Mg–Mg) is between dodecahedral sites linked via an edge-shared tetrahedron, i.e. unusually between third nearest cation neighbours. Figure 3 shows part of the garnet structure, including the dodecahedral framework and the SiO₄ tetrahedra, and highlights this particular interaction. In contrast, the nearest-neighbour and second-nearest-neighbour cation interactions are small. We have carried out a set of calculations for Py₅₀Gr₅₀ with the potentials used in the present study and our results regarding these interactions are in line with those of Bosenick et al. (2000).

Table 2 Calculated hybrid interatomic potentials^a; $C_{\text{eff}} = 0$ in all cases

Garnet	A_{eff}	ρ_{eff}
Py ₂₅ Gr ₇₅	1088.70	0.3359
Py ₅₀ Gr ₅₀	1119.95	0.3258
Py ₇₅ Gr ₂₅	1210.67	0.3124

^a A_{eff} in eV, ρ_{eff} in Å

As already mentioned, all polyhedra in the garnet structure are distorted from “ideal” geometry. Bosenick et al. (2000) have emphasized that the three-dimensional polyhedral network constrains the structure such that rigid-unit modes involving rigid rotations of the polyhedra are not allowed. Any tetrahedral rotation must be accompanied by a simultaneous distortion of the tetrahedra and octahedra. A consequence of these rigid-unit modes is that when an X-site cation is replaced in an end-member compound, all polyhedra are distorted relative to their shape in the end member, and the largest distortion takes place in the two tetrahedra which share edges with the dodecahedron containing the new cation. Bosenick et al. (2000) have used such arguments to rationalize the unfavourable third-neighbour interaction in the dilute limit. This involves two X-sites in dodecahedra corner-shared to the same tetrahedron. For two Ca cations in a pyrope host the tetrahedron is compressed between the two dodecahedra and for two Mg cations in grossular the tetrahedron is expanded. In more concentrated solutions Mg–Mg and Ca–Ca third-nearest-neighbour cation pairs remain energetically unfavourable.

For $\text{Py}_{50}\text{Gr}_{50}$, 15 different arrangements of Mg and Ca atoms were examined (for a more detailed Monte Carlo study see Lavrentiev pers. comm.). The first of these (configuration 1) avoided all energetically unfavourable Mg–Mg and Ca–Ca third-nearest-neighbour pairs [i.e. Mg ions in fractional coordinates at $(1/8, 0, 1/4)$, $(5/8, 1/2, 3/4)$, $(7/8, 1/2, 1/4)$ and $(3/8, 0, 3/4)$ with symmetry-related atoms at (z, x, y) and (y, z, x)]. Of the remaining configurations three were selected at random and the remainder selected to give a range of first, second- and third-nearest neighbours to the substitution X-site. In six cases, the unit cell was doubled in one direction to produce a tetragonal supercell in which it was possible to surround one X-site with two third-nearest cation neighbours of different types. Configuration 1 was the lowest in energy. The others were higher in energy typically by only 1 or 2 kJ mol^{-1} , suggesting, consistent with the work of Bosenick et al. (2000), that configurations containing unfavourable Mg–Mg and Ca–Ca third-neighbour interactions are nevertheless energetically accessible at elevated temperatures, such as those in trace-element solid-melt partitioning experiments. This is consistent with the Monte Carlo study of Lavrentiev et al. (pers. comm.); experimentally Bosenick et al. (1999) have shown that the observed extent of local Ca–Mg ordering is a function of garnet synthesis temperature.

Calculated lattice parameters for the lowest energy configuration (1) of $\text{Py}_{50}\text{Gr}_{50}$ ($a = b = c = 11.592 \text{ \AA}$) are 0.014 Å higher than expected from linear interpolation of the cell edges of simulated end members Py and Gr. Our calculated positive volume of mixing,

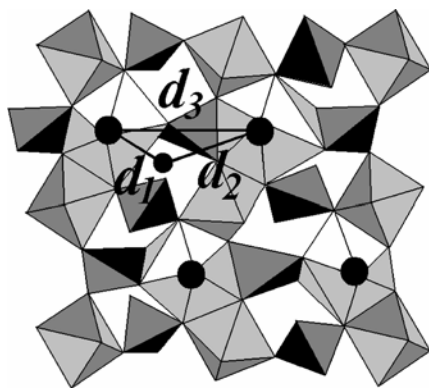


Fig. 3 Detail of the structure of pyrope–grossular garnet, showing the SiO_4 tetrahedra, AlO_6 octahedra and Mg/Ca cations. The dodecahedra surrounding the Mg/Ca atoms are not included for clarity. The first-, second- and third-nearest neighbour cation–cation distances are highlighted. Unusually, the third-nearest neighbour interaction between cations at the centre of two dodecahedra that share edges with the same SiO_4 tetrahedron is markedly repulsive for like cations. For further discussion see text

$0.2 \text{ cm}^3 \text{ mol}^{-1}$, from the lowest energy configuration, is in excellent agreement with experimental data (see Bosenick and Geiger 1997); all the configurations we used gave positive values of ΔV_{mix} broadly similar to this.

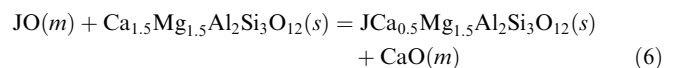
Trace element defect calculations and solution energies

Simulated structures were used as a basis for defect energy calculations. In every computational run, one or more defects was introduced into the crystal, e.g. for homovalent substitution, one divalent cation at the X-site of a perfect garnet lattice was replaced by one divalent trace element cation. Initial, unrelaxed defect energies, $U_{\text{def},i}$, were calculated without allowing any atoms to move. The total energy of the defective system was then minimized by allowing the surrounding ions to relax to accommodate the misfit cation(s). Positions of cores and shells of ions around the introduced defect(s) were optimized using the two-region approach (Catlow and Mackrodt 1982). The inner region containing the defect(s) typically contained 400 ions. Final defect energies after relaxation, $U_{\text{def},f}$, were obtained at convergence.

We simulated incorporation of divalent and trivalent cations into garnets with compositions $\text{Py}_{25}\text{Gr}_{75}$, $\text{Py}_{50}\text{Gr}_{50}$ and $\text{Py}_{75}\text{Gr}_{25}$ using hybrid X-site potentials, and into garnets of compositions $\text{Py}_4\text{Gr}_{96}$, $\text{Py}_{50}\text{Gr}_{50}$ and $\text{Py}_{96}\text{Gr}_4$ using discrete Mg and Ca sites. In the discrete case, for composition $\text{Py}_{50}\text{Gr}_{50}$ we examined substitutions for different local Mg–Ca distributions around the central X-site in order to study explicitly the effects of local X-site ordering on the energetics of trace-element incorporation, as discussed below. This included all possible orderings of the four nearest-neighbours and two third-neighbours orderings (and combinations thereof). In addition, we examined a number of orderings of the eight second neighbours, which preliminary calculations showed, have little effect on the overall solution energies.

For heterovalent substituents, to ensure overall charge balance, a second trace element was inserted simultaneously into the crystal, in one of the nearest-neighbour cation sites. Previous work (Purton et al. 1997a) has demonstrated the importance of defect association in forsterite and diopside. Initial simulations on end-member garnets (Van Westrenen, unpublished data) showed that association of defects lowers the final defect energy of any trivalent trace element in any of the end-member garnets by an additional 57–66 kJ mol^{-1} with respect to isolated defects. Thus we present results here only for associated defects. For the trivalent trace cations studied here (REE and Sc) a Li cation was placed on the adjacent (nearest-neighbour) X-site. This choice of compensating defect has been shown to be the most energy-efficient for these elements in end-member garnets by Van Westrenen et al. (2000a). For more details of the computational procedure, see Van Westrenen et al. (2000a).

The difference between initial and final defect energies is called the relaxation energy, U_{rel} . This energy is analogous to U_{strain} in Eq.(1) and for a particular trace element is a function only of the properties of the garnet crystal. Blundy and Wood (1994) assumed that U_{strain} is equal to the total energy involved in the mineral-melt exchange process. The limitations of this assumption are discussed by Purton et al. (1996). The actual partitioning process in mineral-melt systems involves (1) removal of a trace element (plus accompanying charge-balancing ions) from the melt, (2) incorporation of the trace element(s) in the mineral structure, and (3) insertion of one or more substituted host cations into the melt. Our defect calculations take account of the second process. To take some account of the first and last processes we have also calculated trace-element solution energies (U_{sol}), making a simple assumption about the melt environment. For homovalent substitutions, process (1) through (3) can be described by the substitution reaction (in this case for trace element J^{2+} replacing a Ca in $\text{Py}_{50}\text{Gr}_{50}$ with discrete Ca and Mg sites):



In Eq.(6), (*m*) and (*s*) refer to the melt and solid phase, respectively. As discussed by Van Westrenen et al. (2000a), we approximate the energy associated with Eq. (6), U_{sol} , by

$$U_{\text{sol}} = U_{\text{def},r}(\text{J}) + U_{\text{lat}}(\text{CaO}) - U_{\text{lat}}(\text{JO}) \quad (7)$$

where U_{lat} denotes lattice energy. In applying Eq.(7), we thus assume that the local environments of Ca^{2+} and J^{2+} in a melt are equivalent to their environments in the corresponding solid binary oxides (i.e., CaO and JO). Lattice energies for the binary oxides, obtained with the same interionic potentials used for the garnet simulations, are given in Allan et al. (2001). For garnets with hybrid X-sites, the cation(s) released into the melt are themselves hybrids. Lattice energies for the corresponding hybrid binary oxides were calculated as a weighted average of the lattice energies of CaO and MgO. Analogous equations can be constructed for the partitioning process of trivalent trace elements (see Eqs. 4 and 7 in Van Westrenen et al. 2000a), again assuming that the local environments of J^{3+} and Li are equivalent to their environments in the corresponding solid binary oxides (J_2O_3 and Li_2O). The effects of other assumptions as to local melt environments have been discussed extensively for the end-member compounds in Van Westrenen et al. (2000a). Finally, we stress that although all the simulations reported in this paper are in the static limit, it is known that defect energies in this limit are in close agreement with defect enthalpies at elevated temperatures (Taylor et al. 1997).

Results and discussion

Garnets with hybrid X-sites

In this section we discuss the results for our two types of simulations in turn, starting with U_{rel} and U_{sol} for trace elements entering the hybrid X-sites of garnets $\text{Py}_{75}\text{Gr}_{25}$, $\text{Py}_{50}\text{Gr}_{50}$, and $\text{Py}_{25}\text{Gr}_{75}$. Table 3 gives the calculated values of U_{rel} and U_{sol} for divalent and trivalent trace

elements entering these mixtures, together with end-member data for pure Py and Gr.).

In Fig. 4, these energies are plotted against trace element radius. The parabolic dependence of both U_{rel} and U_{sol} is apparent in all garnets for both divalent and trivalent cations. The curved lines in Fig. 4 are non-linear least-squares fits of both U_{rel} and U_{sol} to the form of the Brice equation (Eq. 1). Best-fit parameters r_0 and E_X are given in Tables 4 and 5 for relaxation and solution energies, respectively. Figs. 5a and b show the variations in r_0 and E_X along the Py–Gr join for relaxation and solution energies.

Figure 5a shows that for relaxation energies, the optimum ionic radius for trivalent cations, $r_0(3+)$, is significantly larger (by 0.04 – 0.07 Å) than r_0 for divalent cations, $r_0(2+)$. This was also observed in our end-member study (Van Westrenen et al. 2000a). The solution energy data, however, show significantly different behaviour, with $r_0(3+) < r_0(2+)$. In our experiments, $r_0(3+)$ is always around 0.05 Å smaller than $r_0(2+)$, although the latter is rather poorly constrained (e.g. Van Westrenen et al. 1998). The effective Young's moduli for divalent substitutions onto the X-site, $E_X(2+)$, are much smaller than $E_X(3+)$ for both relaxation and solution energies. For example, U_{sol} data for $\text{Py}_{75}\text{Gr}_{25}$ show that E_X increases from 363 ± 21 GPa (divalent trace elements) to 562 ± 34 GPa (trivalent elements). This is entirely consistent with results from our partitioning experiments and with theoretical considerations (e.g. Van Westrenen et al. 2000a; see also Hazen and Finger 1979). The r_0 values show that U_{sol} data are most consistent with experimental observations. This reinforces the notion that

Table 3 Relaxation and solution energies in garnets along the pyrope–grossular join, using hybrid interatomic potentials^a

Trace element ^b	Py ₁₀₀		Py ₇₅ Gr ₂₅		Py ₅₀ Gr ₅₀		Py ₂₅ Gr ₇₅		Gr ₁₀₀	
	U_{rel}	U_{sol}	U_{rel}	U_{sol}	U_{rel}	U_{sol}	U_{rel}	U_{sol}	U_{rel}	U_{sol}
Divalent cations										
Ni	0.22	2.64	8.74	-17.4	26.3	-16.9	49.4	-0.06	76.1	29.8
Mg	0.00	0.00	6.27	-21.7	21.9	-22.6	43.5	-6.79	68.9	22.3
Co	0.46	-6.64	3.49	-30.1	16.7	-32.3	36.3	-17.6	60.0	10.7
Fe	2.39	-6.03	1.04	-32.8	10.6	-37.7	27.1	-25.2	48.2	1.24
Mn	13.6	0.29	1.07	-33.6	1.62	-44.4	10.8	-36.7	25.7	-14.1
Ca	95.6	70.0	45.9	17.9	17.7	-7.93	3.91	-12.5	0.00	0.00
Eu	262	213	164	143	98.7	101	55.4	83.7	27.7	85.2
Sr	268	206	168	136	101	95.5	56.6	78.0	28.3	79.9
Ba	497	470	351	379	246	318	170	284	115	272
Trivalent cations										
Sc	279	87	271	28.7	279	11.8	308	32.0	348	82.0
Lu	271	109	234	34.0	219	4.92	230	13.5	256	54.0
Yb	273	117	233	40.2	215	9.62	224	16.7	248	56.0
Ho	284	134	233	52.8	206	18.4	209	21.8	228	58.0
Gd	307	170	240	81.0	201	41.4	194	39.6	206	71.3
Eu	315	178	244	88.0	201	47.1	192	44.1	201	74.7
Nd	350	220	263	122	207	76.5	187	68.6	189	94.9
La	420	287	307	181	230	128	194	113	183	133

^a All energies in kJ mol^{-1} . Lattice energies used for calculation of solution energies from Allan et al. (2001)

^b All trivalent cations are charged-balanced by a coupled Li substitution on adjacent X-site

Fig. 4a–d Variation of calculated relaxation and solution energies along the pyrope-grossular join using hybrid interatomic potentials. **a** 2+ relaxation energies. **b** 3+ relaxation energies. **c** 2+ solution energies. **d** 3+ solution energies. Curves are non-linear least-squares fits of the data to Eq. (1). Data from Table 3, ionic radii from Shannon (1976)

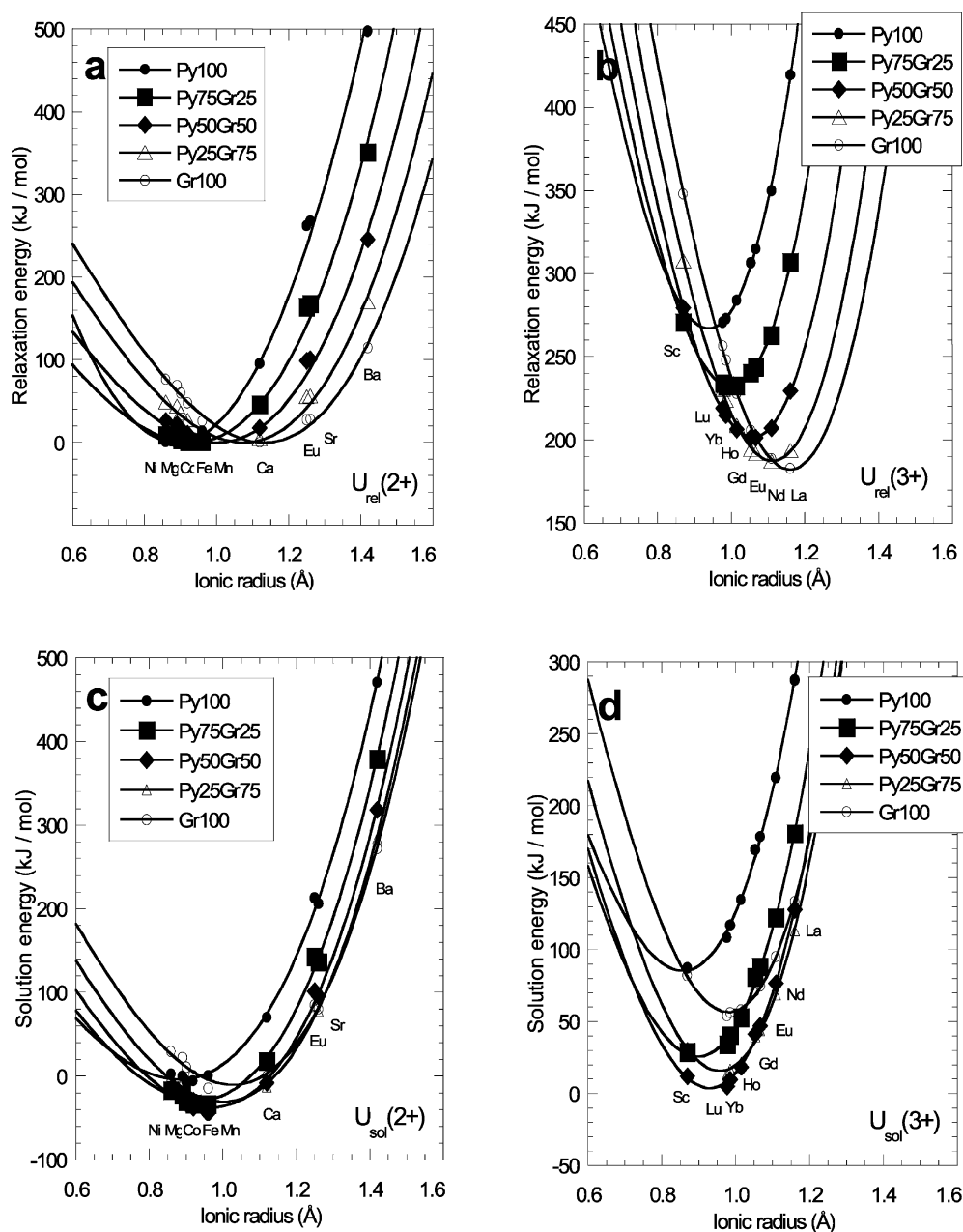


Table 4 Fits of hybrid-potential relaxation energy data (Table 3) to the Brice equation (Eq. 1)^a. Values in parentheses are one standard deviation of last digit

Garnet	2+ defects		3+ defects	
	r_0^a	E_X	r_0	E_X
Py ₁₀₀	0.89(1)	401(14)	0.938(3)	748(22)
Py ₇₅ Gr ₂₅	0.93(1)	321(9)	0.999(1)	679(14)
Py ₅₀ Gr ₅₀	1.00(1)	300(10)	1.059(1)	621(12)
Py ₂₅ Gr ₇₅	1.07(1)	296(11)	1.112(3)	574(15)
Gr ₁₀₀	1.12(1)	289(14)	1.160(5)	541(19)

^a r_0 in Å, E_X in GPa

Table 5 Fits of hybrid-potential solution energy data (Table 3) to the Brice equation (Eq. 1)^a. Values in parentheses are one standard deviation of last digit

Garnet	2+ defects		3+ defects	
	r_0^a	E_X	r_0	E_X
Py ₁₀₀	0.88(2)	350(21)	0.857(12)	551(39)
Py ₇₅ Gr ₂₅	0.93(1)	363(21)	0.899(8)	562(34)
Py ₅₀ Gr ₅₀	0.97(1)	371(21)	0.929(6)	572(30)
Py ₂₅ Gr ₇₅	1.00(1)	376(21)	0.957(4)	581(21)
Gr ₁₀₀	1.03(1)	378(22)	0.981(3)	580(23)

^a r_0 in Å, E_X in GPa

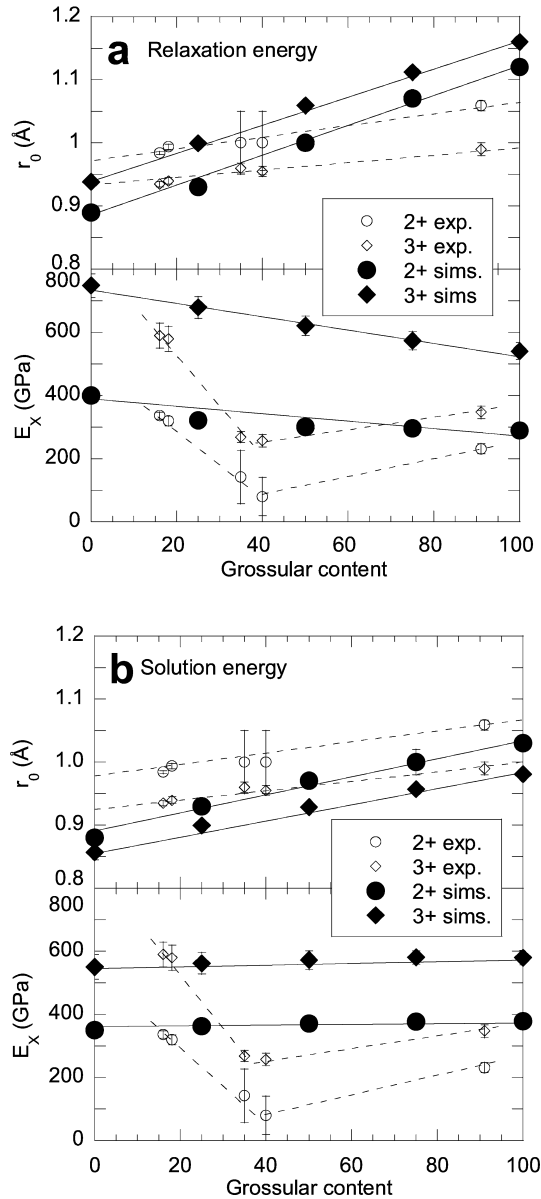


Fig. 5a, b Variation of fit parameters r_0 and E_X for divalent and trivalent trace elements along the Py–Gr join using hybrid interionic potentials. **a** Fits to relaxation energy data (see Table 4). **b** Fits to solution energy data (see Table 5). Error bars are $\pm 1\sigma$. Open symbols are fits to experimental data (Fig. 1b) shown for comparison

U_{sol} , rather than U_{rel} , is the energy most appropriate for models of mineral–melt partitioning energetics (Van Westrenen et al. 2000a). Variations in U_{sol} should therefore be most amenable to comparison with variations in experimental D values.

Both the position of the minimum energy and the curvature of the plots, given by their effective Young’s moduli E , vary systematically along the Py–Gr join (Fig. 5a,b). For solution energies, both $r_0(2+)$ and $r_0(3+)$ increase linearly, while $E_X(2+)$ and $E_X(3+)$ appear approximately constant. The increase in r_0 with increasing Ca content for both divalent and trivalent cations is in agreement with both experiment (Fig. 1b)

and crystallographic data on variations in $\langle X\text{–O} \rangle$ distances in garnets (e.g. Armbruster et al. 1992; Ganguly et al. 1993). The constancy of E_X , however, is not consistent with experimental data [which show $E_X(\text{Py}) > E_X(\text{Gr})$, Van Westrenen et al. 1999]. This will be discussed further in the following section.

It is clear from Fig. 5 that trends in r_0 and E_X for garnets with hybrid X-sites do not show anomalous behaviour along the Py–Gr join. No anomalously low E_X values exist for intermediate garnets. The presence of X-sites in intermediate Py–Gr garnets showing hybrid behaviour, with properties intermediate between Mg and Ca X-sites, cannot explain the behaviour observed experimentally (Fig. 1b).

Garnets with discrete Mg and Ca sites

For our simulations of divalent trace elements substituting into Gr_{100} , $\text{Py}_4\text{Gr}_{96}$, $\text{Py}_{96}\text{Gr}_4$, and Py_{100} garnets with discrete Ca and Mg sites, $U_{\text{def,f}}$, U_{rel} and U_{sol} are summarized in Table 6. In this table elements are listed in order of increasing ionic radius. For substitution at a Mg site, the relaxation energies of trace elements smaller than Ca^{2+} are all larger in $\text{Py}_4\text{Gr}_{96}$ (where all first, second and third neighbours of the Mg are Ca in a primitive unit cell) than in the end-member pyrope itself. The reverse is true for Ca^{2+} itself and larger cations. For substitution at a Ca site, the relaxation energies for all elements are larger in $\text{Py}_{96}\text{Gr}_4$ (where all first, second and third neighbours of the Ca are Mg) than in pure grossular.

Calculated Mg–O bond lengths in $\text{Py}_4\text{Gr}_{96}$ are only slightly larger than in pyrope, and the calculated Ca–O interatomic distances in $\text{Py}_{96}\text{Gr}_4$ are only slightly smaller than those in grossular, in keeping with the results of Bosenick et al. (2000). Mg^{2+} ions thus preserve largely pyrope-type and Ca^{2+} ions a predominant grossular-type environments even in this dilute limit. As emphasized by Bosenick et al. (2000), these local cation–oxygen bond lengths are very different from averaged X–O bond distances such as those obtained from X-ray diffraction for compositions such as these. Our conclusions are not in line with those of Quartieri et al. (1995), who suggest, from a XANES study of the local crystal environment of Ca in garnets, that the Ca environment in Mg-rich garnets is similar to the Mg environment in the same garnets, and different from the Ca environment in pure grossular.

Similarly, the new trace element optimizes its local environment, i.e. interatomic distances and orientations adjust locally to the most energetically favourable values. The garnet structure has no degrees of freedom to permit local tilting or rotation of rigid AlO_6 octahedra or SiO_4 tetrahedra since there are no rigid unit modes. Any tilting or rotation of a tetrahedron or octahedron in the framework to accommodate a trace-element cation in a resized dodecahedral X site would require the same motion of all polyhedra in the

framework structure, and the collective distortion involved would be high in energy. An alternative, much lower in energy, is distortion, primarily of the tetrahedra and octahedra which are direct neighbours of the trace element.

Small changes in environment can nevertheless lead to relatively large changes in defect thermodynamics. It is clear from Table 6 that at the Mg site the ions equal in size or smaller than Mn^{2+} have larger relaxation energies in $\text{Py}_4\text{Gr}_{96}$, but the overall defect energy is lower for all ions equal in size or larger than Mg^{2+} and only higher for Ni^{2+} , which is slightly smaller than Mg^{2+} . The lowering in energy is particularly marked for the largest ions (Ba^{2+} and Sr^{2+}). This arises because the cation exchange process (Purton et al. 1996) for an iso-valent substitution involves both the strain (relaxation) energies and the replacement of one set of short-range interaction energies with another. The trends are consistent with a Mg site effectively slightly larger in $\text{Py}_4\text{Gr}_{96}$ than in pyrope.

For substitution at Ca^{2+} , relaxation energies are larger for all elements in $\text{Py}_{96}\text{Gr}_4$ and defect energies lower for elements smaller than Mn^{2+} and larger for the remainder. This is consistent with a Ca site effectively slightly smaller in $\text{Py}_{96}\text{Gr}_4$ than in grossular.

In most cases, the changes in the defect energy from end-member to dilute mixture, involving both relaxation and interaction contributions, are much larger than those in the relaxation energies. For example for Sr^{2+} at

Ca sites, there is a difference in 6 kJ mol^{-1} in U_{rel} between $\text{Py}_{96}\text{Gr}_4$ and grossular, but $U_{\text{def},f}$ is over 50 kJ mol^{-1} higher in $\text{Py}_{96}\text{Gr}_4$. This is even more marked for the larger Ba^{2+} .

The difference in $U_{\text{def},f}$ is carried over into the solution energies (see Eq. 7) and so the solution energies in Table 6 show some remarkable features. The calculated solution energy for the largest ion, Ba^{2+} , at a Mg site in $\text{Py}_4\text{Gr}_{96}$ is comparable to that at a Ca site in grossular itself. The lowest value of U_{sol} for the smallest ion, Ni^{2+} , in Table 6 is at a Ca^{2+} site in $\text{Py}_{96}\text{Gr}_4$ and is considerably lower than for Ni^{2+} substitution in pyrope and in grossular.

The results in Table 6 suggest that it is important to consider local orderings in detail. We have therefore considered all possible nearest-neighbour and third-neighbour orderings and a large number of second-neighbour orderings on dopant incorporation in $\text{Py}_{50}\text{Gr}_{50}$. Table 7 collects together the lowest solution energies for Ni^{2+} , Fe^{2+} , Mn^{2+} , Sr^{2+} and Ba^{2+} in $\text{Py}_{50}\text{Gr}_{50}$.

Consider first the incorporation of Ba^{2+} . The nature of the four first cation neighbours influences the solution energy U_{sol} in the same ways as for the more dilute solutions. In addition, the makeup of the third-nearest neighbour shell has a striking influence on the defect energies and thus, via Eq. (7) on the solution energies. If substitution of the X-site cation removes an unfavourable third-neighbour interaction by introducing a size

Table 6 Calculated $U_{\text{def},f}$, U_{rel} , and U_{sol} in pyrope, grossular, $\text{Py}_4\text{Gr}_{96}$, and $\text{Py}_{96}\text{Gr}_4$ solid solutions with distinct Mg and Ca sites^a

Substituent	Substitution on Mg site						Substitution on Ca site					
	Py ₁₀₀			Py ₄ Gr ₉₆			Gr ₁₀₀			Py ₉₆ Gr ₄		
	$U_{\text{def},f}$	U_{rel}	U_{sol}	$U_{\text{def},f}$	U_{rel}	U_{sol}	$U_{\text{def},f}$	U_{rel}	U_{sol}	$U_{\text{def},f}$	U_{rel}	U_{sol}
Ni	-33.4	0.22	2.64	-32.2	3.79	3.84	-523	76.1	29.8	-615	85.5	-61.6
Mg	0.00	0.00		0.00	0.00	0.00	-495	68.9	22.3	-582	77.6	-64.6
Co	31.4	0.46	-6.64	23.0	4.06	-15.0	-468	60.0	10.7	-551	67.9	-71.6
Fe	100	2.39	-6.03	81.9	5.82	-24.1	-410	48.2	1.24	-483	54.8	-71.7
Mn	243	13.6	0.29	204	16.2	-38.8	-288	25.7	-14.1	-341	29.8	-66.9
Ca	587	95.6	70.0	494	91.3	-22.9		0.00	0.00		0.00	0.00
Eu	940	262	213	791	240	64.1	295	27.7	85.2	348	33.7	138
Sr	923	268	206	776	245	58.8	280	28.3	79.9	332	34.5	132
Ba	1433	497	470	1216	448	253	718	115	272	838	134	392

^a All energies in kJ mol^{-1} . Lattice energies used for calculation of solution energies from Allan et al. (2001)

Table 7 Calculated lowest energy solution energies (U_{sol}) in pyrope (Py), grossular (Gr) and $\text{Py}_{50}\text{Gr}_{50}$ ^a

Substituent	U_{sol} (Py)	U_{sol} (Gr)	U_{sol} (Py ₅₀ Gr ₅₀)	X ^b	Nearest neighbours ^b	Third nearest neighbours ^b
Ni	2.64	29.8	-50	Ca	4 Mg	2 Ca
Fe	-6.03	1.24	-60	Ca	2 Mg + 2 Ca	2 Ca
Mn	0.29	-14.1	-51	Ca	2 Mg + 2 Ca	2 Ca
Sr	206	79.9	56	Mg	4 Ca	2 Mg
Ba	470	272	252	Mg	4 Ca	2 Mg

^a All energies in kJ mol^{-1} . Lattice energies used for calculation of solution energies from Allan et al. (2001)

^b X specifies the cation replaced in $\text{Py}_{50}\text{Gr}_{50}$. Subsequent columns denote the first and third nearest neighbours of X in the solid solution

mismatch between the ions in this position, then the defect and solution energies are lower, as the overall compression or extension of the tetrahedron between the two dodecahedra is reduced.

For example, U_{sol} for replacement of an Mg^{2+} by Ba^{2+} is $\approx 20\text{--}40\text{ kJ mol}^{-1}$ lower, depending on whether the first neighbours are all Mg or all Ca, with lower values for Ca neighbours. This is not unexpected, since the X-site in this case will be slightly larger, consistent with the trends noted in Table 6. The solution energy varies by an even larger figure – as much as 75 kJ mol^{-1} – with the nature of the third neighbour. Overall, the lowest solution energy for Ba^{2+} substitution at an Mg site is 252 kJ mol^{-1} and at a Ca site 290 kJ mol^{-1} . These values are remarkable as they indicate that the most favourable substitution site for the large Ba^{2+} in $\text{Py}_{50}\text{Gr}_{50}$ is not necessarily a Ca^{2+} site as expected from Goldschmidt's first rule (Goldschmidt 1937). Substitution in $\text{Py}_{50}\text{Gr}_{50}$ can take place at an Mg site depending on the local environment of such a site. For comparison, the solution energies of Ba^{2+} in pure pyrope and grossular are 470 and 272 kJ mol^{-1} , respectively (Van Westrenen et al. 2000a). The variation in calculated solution energy along the pyrope–grossular join is thus non-linear with values for $\text{Py}_{50}\text{Gr}_{50}$ lower than those for either end member. In addition, the possibility of substitution at more than one sublattice will lower the free energy of substitution because of the larger configurational entropy change accompanying the disordering of two sublattices rather than one. All these factors result in a predicted higher solubility of Ba^{2+} in $\text{Py}_{50}\text{Gy}_{50}$ than that expected from an interpolation between the end-member compounds.

The same remarks apply to Sr^{2+} substitution. Once again, Sr^{2+} is more soluble in $\text{Py}_{50}\text{Gr}_{50}$ than in pyrope or grossular, with a value of 56 kJ mol^{-1} of U_{sol} at a Mg site, compared to 80 kJ mol^{-1} in grossular and 206 kJ mol^{-1} in pyrope.

A similar set of arguments can be used to rationalize the defect energies for Ni^{2+} , remembering that Ni^{2+} is only slightly smaller than Mg^{2+} . Introducing an Ni^{2+} at an X-site where all four third neighbours are Ca^{2+} is favoured relative to a site with two or four Mg^{2+} third neighbours due to the removal of the effective repulsion between an ion (Ni^{2+}) and a third neighbour (Mg^{2+}) similar in size. This is sufficiently important for the lowest solution energy for Ni^{2+} (-50 kJ mol^{-1}) to be for replacement of a Ca^{2+} rather than substitution of a Mg^{2+} (lowest energy $+4.5\text{ kJ mol}^{-1}$). Once more this represents a deviation from Goldschmidt's first rule. We have also carried out calculations for Fe^{2+} and Mn^{2+} in $\text{Py}_{50}\text{Gy}_{50}$. These lie between Mg^{2+} and Ca^{2+} in size but are closer to Mg^{2+} . Like Ni^{2+} , these ions are predicted to substitute at a Ca^{2+} site which possesses two Ca^{2+} third neighbours, and solution energies are lower than in either of the end-member compounds.

It is worth noting that though there is a correlation between the relaxation and defect energies, the variation in the relaxation energies themselves is not sufficient to

make the two types of X-site energetically indistinguishable. The variation in the defect energies is larger (as with Table 6) due to the additional interaction term and, together with the difference in lattice energy of CaO and MgO, is responsible for the solution energies at the two types of site to become comparable.

We have carried out calculations of defect energies for trace elements in $\text{Py}_{50}\text{Gy}_{50}$ for environments varying second as well as first and third neighbours. There are eight such second neighbours and these are located in two dodecahedra, one of which is edge- and the other corner-shared to the same tetrahedron. Changes in the second neighbour compensate somewhat for first-neighbour changes. For example, for identical host cation and third neighbours, defect energies (and thus solution energies) with two Mg, two Ca first neighbours and eight Ca second neighbours are very close to those with four Ca first neighbours and eight Mg second neighbours. Overall, our conclusions regarding the importance of the third neighbours are unchanged.

Figure 6 summarizes our overall conclusions. All five trace-element cations, Ni^{2+} , Fe^{2+} , Mn^{2+} , Sr^{2+} and Ba^{2+} appear more soluble in $\text{Py}_{50}\text{Gy}_{50}$ than in either pyrope or grossular end members. The discussion above suggests this is due to (1) the slight overall change in size of the X-sites themselves in the solid solution compared to the end members and (2) the increased scope for removal of unfavourable interactions between third nearest neighbours of the same size. Thus a large ion may substitute preferentially for a Mg^{2+} (with two Mg^{2+} third neighbours) rather than a Ca^{2+} and a small ion may substitute preferentially for a Ca^{2+} (with two Ca^{2+} third neighbours) rather than for a Mg^{2+} . This suggests that the simple idea of an optimum cation radius for substitution of a given ion which is transferable from one system to another, as suggested by Goldschmidt, breaks down for the garnet solid solution. It also provides an explanation for the anomalous trace-element partitioning behaviour of the solid solution, since the net result from a partitioning point of view is a broadening of the solution energy vs. ionic radius curve with the lower curvature suggesting an apparent ‘softening’ of the structure (Fig. 6b) and a lower site modulus. The minimum in the curve for $\text{Py}_{50}\text{Gy}_{50}$ in Fig. 6b lies between Ca^{2+} and Mg^{2+} , and the curvature and thus the effective Young's modulus are lower than that for either pyrope or grossular.

We have not carried out a comprehensive study of the solution energies of trivalent trace elements substituting into these systems. In this case, the nature of the charge-balancing substitution is an additional factor that influences the resulting energies, so there are even more local configurations to examine. For example, replacing an Mg by an La could be charge-balanced by the insertion of an Li in place of another Mg or Ca in $\text{Py}_{50}\text{Gr}_{50}$, while in pure pyrope Li can only replace Mg. Preliminary results show that the most energy-efficient charge-balancing mechanism involves the replacement of another Ca with Li, and that overall the solution

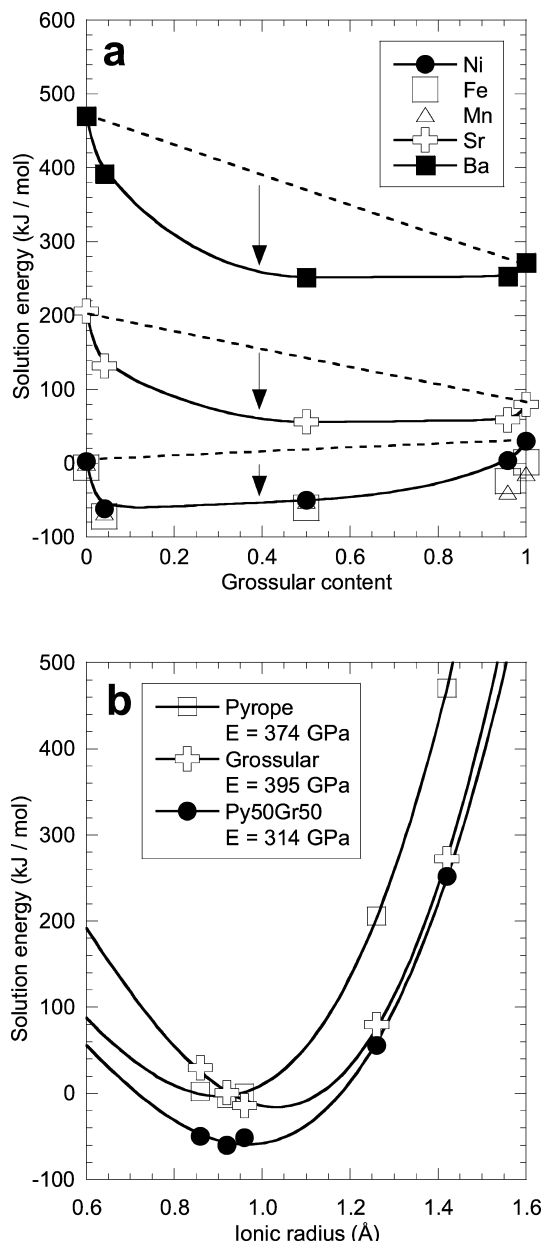


Fig. 6 **a** Variation of solution energies for five divalent trace elements across the pyrope–grossular join, assuming discrete Ca and Mg garnet X-sites. *Arrows* indicate that solution energies in solid solutions are significantly lower than expected from a linear interpolation between end-member values (indicated by the *dotted lines* for Ni, Ba and Sr). **b** Solution energies as a function of ionic radius for pyrope, grossular and Py₅₀Gr₅₀. Curves are non-linear least-squares fits of the data to Eq. (1). Data from Tables 6 and 7, ionic radii from Shannon (1976). Note that the best-fit value of apparent bulk modulus E_X in Py₅₀Gr₅₀ is smaller than the best-fit values for both pure pyrope and pure grossular

energy variation is similar to that for the divalent elements, with solution energies lower in the mixed garnet than in either end member.

Hence, although structurally the Ca and Mg sites clearly remain distinct in the solid solution, energetically they may appear equivalent, depending on the local

environment. EXAFS data on the local relaxation around Yb³⁺ in pure Py and Gr (Quartieri et al. 1999) confirm that the structural relaxation around trace elements in the garnet X-site is extremely localized.

There are other possible alternative explanations of the anomalous partitioning behaviour. Firstly, changes in the melt environment of trace elements (e.g., a change in co-ordination number) can have a marked influence on calculated solution energies and resulting r_0 and E_X values. An explanation for the anomalous behaviour of E_X in Fig. 1b is that the trace-element environment in melt coexisting with the intermediate Py–Gr garnets is different from their environment in the other experiments. This is somewhat unlikely for two reasons. First, all experiments were performed in the same simple system (CMAS), without addition of volatiles. The polymerization of the melts is very similar for all melts reported in Van Westrenen et al. (1999). For example, NBO/T (non-bridging oxygens per tetrahedral cation, a measure of melt polymerization) is in the restricted range 0.7–1.1, and Al / (Al + Si) in the range 0.27–0.43. There is therefore little scope for dramatic variations in melt environment along the Py–Gr join. Secondly, as shown by the examples given above, changes in E_X would be accompanied by changes in r_0 , and these are not observed (Fig. 1b).

A second possibility, brought forward by Van Westrenen et al. (1999), is that the reduced elastic moduli are a precursor effect for a garnet symmetry change (Carpenter and Salje 1998; Boffa Ballaran et al. 1999; Carpenter et al. 1999), possibly accompanied by local Ca–Mg ordering. There is a complete lack of experimental observations on phase transitions in intermediate Py–Gr garnets. IR band softenings observed by Boffa Ballaran et al. (1999) show that intermediate garnets, as opposed to near-end-member Py and Gr, would be prime candidates for such a transition at high pressures. The extensive spectroscopic studies of Merli et al. (1995) and Ungaretti et al. (1995) do suggest that anomalous structural behaviour occurs along the Py–Gr join. However, recent Monte Carlo studies (Lavrentiev pers. comm. 2002) do not appear to show any loss of symmetry at pressures up to 15 GPa. Clearly, X-site ordering and the possibility of phase transitions in Py–Gr mixtures under high pressures require further investigation. Additionally, more spectroscopic data on the actual local environment of trace elements in Py–Gr solid solutions would be highly useful. Quartieri et al. (1999) looked only at pure Py and Gr garnets in their study of the local environment of Yb in garnet, so that there was no possibility of two-site behaviour as only one type X-site cation (Mg or Ca) was present in any experiment.

Finally, there is considerable scope for further computational work. It would be useful to develop general rules of thumb for solid solutions more generally, for heterovalent defects as well as isovalent defects, and analyze a range of solid solutions with and without rigid unit modes. Equations. (6) and (7) make a very simple

assumption regarding the melt environment and energetics of both major and trace cations, and further information here is urgently needed.

Conclusions

We have carried out a wide range of atomistic simulations of trace element incorporation into the X-site of Py–Gr solid solutions. Relaxation energies, defect energies and solution energies were obtained using two different approaches, the first a hybrid, mean-field approach and the second assuming discrete Ca and Mg sites. The hybrid model, which averages out local distortions in the garnet structure, is shown to be inadequate.

Our results using the discrete model suggest that trace elements are more soluble in Py₅₀Gy₅₀ than in either end-member compound. Physically, this is due to small changes in size of the X-sites and the scope for removal of unfavourable interactions between third nearest neighbours of the same size. Depending on the local environment, large ions may substitute preferentially for an Mg²⁺ and small ions for a Ca²⁺ ion. The concept that, for a given cation, there is an optimum radius for a substituent that is transferable from system to system, as suggested by Goldschmidt, appears to fail for the pyrope–grossular solid solution. The solubilities of trace elements in Py₅₀Gy₅₀ also provide an explanation for the anomalous trace-element partitioning behaviour of the solid solution.

Acknowledgements We thank M. Carpenter, T. Boffa Ballaran and F. Brouwer for their informed insights, and two anonymous reviewers for their critical comments, which greatly improved our manuscript. W.v.W acknowledges financial support from the EU (contract ERBFMBICT 971991) and Dutch VSB Foundation, technical input from Dr. D. Bergkamp, and cross-field support from Prof. M. Overmars. JDB is grateful to the Royal Society for a University Research Fellowship. An EPSRC grant GR/M53899, and JREI awards, and NERC grant GR3/09772 supported parts of this work.

References

- Allan NL, Blundy JD, Purton JA, Lavrentiev MYu, Wood BJ (2001) Trace element incorporation in minerals and melts. In: Geiger CA (ed) *Solid solutions in silicate and oxide systems*, vol 3. Papp G, Weiszbürg, TG (Series eds.) *European Mineralogical Union Notes in Mineralogy*, Eötvös University Press, pp 251–302
- Armbruster T, Geiger CA, Lager GA (1992) Single-crystal X-ray structure of synthetic pyrope almandine garnets at 100 and 293 K. *Am Mineral* 77: 512–521
- Beattie P (1994) Systematics and energetics of trace-element partitioning between olivine and silicate melts: implications for the nature of mineral/melt partitioning. *Chem Geol* 117: 57–71
- Blichert-Toft J, Albarède F, Kornprobst J (1999) Lu–Hf isotope systematics of garnet pyroxenites from Beni Bousera, Morocco: implications for basalt origin. *Science* 283: 1303–1306
- Blundy JD, Wood BJ (1994) Prediction of crystal–melt partition coefficients from elastic moduli. *Nature* 372: 452–454
- Boffa Ballaran T, Carpenter MA, Geiger CA, Koziol AM (1999) Local structural heterogeneity in garnet solid solutions. *Phys Chem Miner* 26: 554–569
- Bosenick A, Dove MT, Geiger CA (2000) Simulation studies on the pyrope–grossular garnet solid solution. *Phys Chem Miner* 27: 398–418
- Bosenick A, Dove MT, Heine V, Geiger CA (2001) Scaling of thermodynamic mixing properties in garnet solid solutions. *Phys Chem Minerals* 28: 177–187
- Bosenick A, Geiger CA (1997) Powder X-ray diffraction study of synthetic pyrope–grossular garnets between 20 and 295 K. *J Geophys Res* 102: 22649–22657
- Bosenick A, Geiger CA, Phillips BL (1999) Local Ca–Mg distribution of Mg-rich pyrope–grossular garnets synthesized at different temperatures revealed by ²⁹Si MAS NMR spectroscopy. *Am Mineral* 84: 1422–1432
- Bosenick A, Geiger CA, Schaller T, Sebald A (1995) A ²⁹Si MAS NMR and IR spectroscopic investigation of synthetic pyrope–grossular garnet solid solutions. *Am Mineral* 80: 691–704
- Bourdon B, Zindler A, Elliott T, Langmuir CH (1996) Constraints on mantle melting at mid-ocean ridges from global ²³⁸U–²³⁰Th disequilibrium data. *Nature* 384: 231–235
- Brice JC (1975) Some thermodynamic aspects of the growth of strained crystals. *J Crystal Growth* 28: 249–253
- Carpenter MA, Salje EKH (1998) Elastic anomalies in minerals due to structural phase transitions. *Eur J Mineral* 10: 693–812
- Carpenter MA, Boffa Ballaran T, Atkinson AJ (1999) Microscopic strain, local structural heterogeneity and the energetics of silicate solid solutions. *Phase Transitions* 69: 95–109
- Catlow CRA, Mackrodt WC (1982) Theory of simulation methods for lattice and defect energy calculations in crystals. In: Catlow CRA, Mackrodt WC (eds) *Computer simulation of solids*. Springer, Berlin Heidelberg New York pp. 3–20
- Dick BG, Overhauser AW (1958) Theory of the dielectric constants of alkali halide crystals. *Phys Rev* 112: 90–103
- Frey FA, Garcia MO, Roden MF (1994) Geochemical characteristics of Koolau Volcano: implications of intershield geochemical differences among Hawaiian volcanoes. *Geochim Cosmochim Acta* 58: 1441–1462
- Gale JD (1997) GULP – a computer program for the symmetry adapted simulation of solids. *Faraday Trans* 93: 629
- Ganguly J, Cheng W, O'Neill HStC (1993) Syntheses, volume, and structural changes of garnets in the pyrope–grossular join: implications for stability and mixing properties. *Am Mineral* 78: 583–593
- Gast PW (1968) Trace element fractionation and the origin of tholeiitic and alkaline magma types. *Geochim Cosmochim Acta* 32: 1057–1086
- Geiger CA (1999) Thermodynamics of (Fe²⁺, Mn²⁺, Mg, Ca)₃Al₂Si₃O₁₂ garnet: an analysis and review. *Mineral Petrol* 66: 271–299.
- Geiger CA (2001) Thermodynamic mixing properties of binary oxide and silicate solid solutions determined by direct measurement: the role of strain. In: Geiger CA (ed) *Solid solutions in silicate and oxide systems*, vol. 3. Papp G, Weiszbürg, TG (series eds) *European Mineralogical Union Notes in Mineralogy*. Eötvös University Press, pp 71–100
- Goldschmidt VM (1937) The principles of the distribution of chemical elements in minerals and rocks. *J Chem Soc* 140: 655–673
- Harte B, Kirkley MB (1997) Partitioning of trace elements between clinopyroxene and garnet: data from mantle eclogites. *Chem Geol* 136: 1–24
- Hazen RM, Finger LW (1979) Bulk modulus–volume relationship for cation–anion polyhedra. *J Geophys Res* 84: 6723–6728
- Hirschmann MM, Stolper EM (1996) A possible role for garnet pyroxenite in the origin of the “garnet signature” in MORB. *Contrib Mineral Petrol* 124: 185–208
- LaTourrette TZ, Kennedy AK, Wasserburg GJ (1993) Thorium–uranium fractionation by garnet: evidence for a deep source and rapid rise of oceanic basalts. *Science* 261: 739–742

- Loubet M, Allègre CJ (1982) Trace elements in orogenic lherzolites reveal the complex history of the upper mantle. *Nature* 298: 809–814
- McKenzie D, O’Nions RK (1991) Partial melt distributions from inversion of rare earth element concentrations. *J Petrology* 32: 1021–1091
- Merli M, Callegari A, Cannillo E, Caucia F, Leona M, Oberti R, Ungaretti L (1995) Crystal-chemical complexity in natural garnets: structural constraints on chemical variability. *Eur J Mineral* 7: 1239–1249
- Onuma N, Higuchi H, Wakita H, Nagasawa H (1968) Trace-element partition between two pyroxenes and the host lava. *Earth Plan Sci Lett* 5: 47–51
- Purton JA, Allan NL, Blundy JD, Wasserman EA (1996) Isovalent trace element partitioning between minerals and melts – a computer simulation model. *Geochim Cosmochim Acta* 60: 4977–4987
- Purton JA, Allan NL, Blundy JD (1997a) Calculated solution energies of heterovalent cations in forsterite and diopside: implications for trace-element partitioning. *Geochim Cosmochim Acta* 61: 3927–3936
- Purton JA, Allan NL, Blundy JD (1997b) Impurity cations in the bulk and the 001 surface of muscovite. *J Mat Chem* 7: 1947–1951
- Purton JA, Blundy JD, Allan NL (2000) Computer simulation of high temperature forsterite-melt partitioning. *Am Mineral* 85: 1087–1091
- Putirka K (1999) Melting depths and mantle heterogeneity beneath Hawaii and the East Pacific Rise: constraints from Na/Ti and rare-earth element ratios. *J Geophys Res* 104: 2817–2829
- Quartieri S, Chaboy J, Merli M, Oberti R, Ungaretti L (1995) Local structural environment of calcium in garnets: a combined structure-refinement and XANES investigation. *Phys Chem Miner* 22: 159–169
- Quartieri S, Antonioli G, Geiger CA, Artioli G, Lottici PP (1999) XAFS characterization of the structural site of Yb in synthetic pyrope and grossular garnets. *Phys Chem Miner* 26: 251–256
- Shannon RD (1976) Revised effective ionic radii and systematic studies of interatomic distances in halides and chalcogenides. *Acta Crystallogr (A)* 32: 751–767
- Shaw DM (1970) Trace-element fractionation during anatexis. *Geochim Cosmochim Acta* 34: 237–243
- Shen G, Forsyth DW (1995) Geochemical constraints on the initial and final depth of melting beneath mid-ocean ridges. *J Geophys Res* 100: 2211–2237
- Shimizu N (1975) Rare-earth elements in garnets and clinopyroxenes from garnet lherzolite nodules in kimberlites. *Earth Plan Sci Lett* 25: 26–32
- Smyth JR, Bish DL (1988) Crystal structures and cation sites of the rock-forming minerals. Allen & Unwin, New York
- Taylor MB, Barrera GD, Allan NL, Barron THK, Mackrodt WC (1997) Free energy of formation of defects in polar solids. *Faraday Discuss* 106: 377–387
- Ungaretti L, Leona M, Merli M, Oberti R (1995) Non-ideal solid-solution in garnet: crystal-structure evidence and modelling. *Eur J Mineral* 7: 1299–1312
- Van Westrenen W, Allan NL, Blundy JD, Lavrentiev MYu, Lucas BR, Purton JA (2003) Dopant incorporation into garnet solid solutions – a breakdown of Goldschmidt’s first rule. *Chem Comm*, in press
- Van Westrenen W, Blundy JD, Purton JA, Wood BJ (1998) Towards a predictive model for garnet-melt trace-element partitioning: experimental and computational results. *Min Mag* 62A: 1580–1581
- Van Westrenen W, Blundy JD, Wood BJ (1999) Crystal-chemical controls on trace-element partitioning between garnet and anhydrous silicate melt. *Am Mineral* 84: 838–847
- Van Westrenen W, Allan NL, Blundy JD, Purton JA, Wood BJ (2000a) Atomistic simulation of trace-element incorporation into garnets – comparison with experimental garnet-melt partitioning data. *Geochim Cosmochim Acta* 64: 1629–1639
- Van Westrenen W, Blundy JD, Wood BJ (2000b) Effect of Fe²⁺ on garnet-melt trace-element partitioning: experiments in FCMAS and quantification of crystal-chemical controls in natural systems. *Lithos* 53: 189–201
- Van Westrenen W, Wood BJ, Blundy JD (2001a) A predictive thermodynamic model of garnet-melt trace-element partitioning. *Contrib Mineral Petrol* 142: 219–234
- Van Westrenen W, Wood BJ, Blundy JD (2001b) HFSE / REE fractionations during partial melting in the presence of garnet: implications for identification of mantle heterogeneities. *Geochim Geophys Geosys* 2, paper 2000GC00133
- Winkler B, Dove M, Leslie M (1991) Static lattice energy minimization and lattice dynamics calculations on aluminosilicate minerals. *Am Mineral* 76: 313–331
- Wood BJ, Blundy JD (1997) A predictive model for rare-earth element partitioning between clinopyroxene and anhydrous silicate melt. *Contrib Mineral Petrol* 129: 166–181